Dynamics of thin metal foils irradiated by moderate-contrast high-intensity laser beams

M. E. Povarnitsyn, N. E. Andreev, P. R. Levashov, K. V. Khishchenko, and O. N. Rosmej

Citation: Phys. Plasmas **19**, 023110 (2012); doi: 10.1063/1.3683687
View online: http://dx.doi.org/10.1063/1.3683687
View Table of Contents: http://pop.aip.org/resource/1/PHPAEN/v19/i2
Published by the American Institute of Physics.

Dynamics of thin metal foils irradiated by moderate-contrast high-intensity laser beams

M. E. Povarnitsyn,[1,a)] N. E. Andreev,[1,2] P. R. Levashov,[1,2] K. V. Khishchenko,[1,2] and O. N. Rosmej[3]
[1]*Joint Institute for High Temperatures RAS, Izhorskaya 13 Bldg. 2, Moscow 125412, Russia*
[2]*Moscow Institute of Physics and Technology (State University), Institutsky lane 9, Dolgoprudny, Moscow 141700, Russia*
[3]*GSI Helmholtzzentrum für Schwerionenforschung GmbH Planckstraße 1, Darmstadt 64291, Germany*

(Received 28 August 2011; accepted 3 January 2012; published online 17 February 2012)

Laser contrast is a crucial parameter in experiments with high-intensity high-energy pulses. For relativistic intensities of the main pulse $\gtrsim 10^{19}$ W/cm^2, even high-contrast beams can produce plasma on the target surface due to a long nanosecond prepulse action which results in an undesirable early smearing of the target. In particular, dynamics of thin foils under the prepulse action is especially important for the laser ion acceleration technique and x-rays generation. To avoid the influence of the long laser prepulse, a thin foil can be arranged in front of the target. The analysis of the multi-stage foil dynamics is performed using a wide-range two-temperature hydrodynamic model, which correctly describes the foil expansion starting from the normal solid density at room temperature. Simulations show that varying the foil thickness, one can diminish the prepulse transmission through the foil material in many orders of magnitude and at the same time provide the total transparency of the foil plasma by the moment of the main high-intensity ultrashort pulse arrival. Modeling of shielded and unshielded target dynamics demonstrates the effectiveness of this technique. However, the prepulse energy re-emission by the shielding foil plasma can be sizable producing an undesirable early heating of the target placed behind the foil. © *2012 American Institute of Physics*. [doi:10.1063/1.3683687]

I. INTRODUCTION

Ultrashort subpicosecond laser irradiation of targets with relativistic pulse intensities $\gtrsim 10^{19}$ W/cm^2 is used in many applications,[1] in particular, for the x-ray sources development and warm dense matter production,[2] particle acceleration,[3] and fast ignition.[4] In these experiments, a very important laser facility parameter is the pulse contrast ratio, which at time t is defined as the ratio of the prepulse intensity $I(t)$ to the peak laser intensity of the main pulse I_{max}. Laser systems based on the chirped pulse amplification technique usually produce two types of prepulses: a relatively low-intensity nanosecond pedestal due to the amplified spontaneous emission and temporal structures on a sub-100 ps time scale.[5] Typically, the contrast ratio at ~1 ns before the main pulse is about 10^{-6} as reported in Ref. 6 and it can be diminished using the plasma mirror technique[3,7] or frequency doubling[2] by a few orders of magnitude. But even for improved contrast of the order of 10^{-8}, which can be produced by modern setups, for the laser pulses of peak intensities $\gtrsim 10^{19}$ W/cm^2, the energy contained in the nanosecond prepulse is sufficient to generate a plasma at the surface of a solid target, well before the main pulse. This changes a lot the dynamics of high-intensity laser-solid interaction[8] and hampers in the application of thin foils and nano-structured targets,[9] which can be destroyed completely by the prepulse action.

Thin foils dynamics under the prepulse action is especially important for the promising design of targets for the laser ion acceleration.[10] On the other hand, a thin foil can be arranged to shield the main target from the laser prepulse impact. In the latter case, the shielding foil of a proper thickness can totally absorb the prepulse till the moment specified. Indeed, the heating of the foil material results in its subsequent rarefaction. This process leads eventually to the electron density drop below the critical value so the plasma shield becomes transparent for the laser beam. The moment of the foil material transparency depends on the laser pulse intensity profile, foil thickness, material used, etc. In the best case, this moment corresponds to the main pulse arrival time.

In this paper, we analyze the metal foil dynamics under the action of a nanosecond prepulse of the intense laser beam using the model.[11] After a short description of the model in Secs. II to IV, the results of simulation of the aluminum thin foil response to a nanosecond prepulse action are presented in Sec. V. The fraction of the laser energy transmitted through the foil is determined together with the estimation of emitted thermal radiation flux. Simulation of shielded and unshielded target dynamics is also performed and discussed. Conclusions are given in Sec. VI.

II. LASER ENERGY ABSORPTION AND REFLECTION

The laser light absorption and reflection can be calculated for an arbitrary profile of high-frequency permittivity by methods of classical electrodynamics. The permittivity is a function of thermodynamic parameters, distribution of

a)Author to whom correspondence should be addressed. Electronic mail: povar@ihed.ras.ru.

which in matter can in turn be obtained from the hydrodynamic equations. Non-equilibrium states of matter under fast heating can be taken into account to some extent in a two-temperature approximation. In general, the laser–matter interaction is governed by several characteristic scales such as wavelength, skin layer depth, and also resonance absorption layer for a *P*-polarized beam.

In one-dimensional approximation, a material permittivity depends on z coordinate only, normal to the target surface so that $\varepsilon = \varepsilon(z)$ and $\varepsilon(z \to -\infty) = 1$. Then, for the *S*-polarization of the laser field, we can write $\tilde{\mathbf{E}} = \mathrm{Re}\{\mathbf{E}\exp(-i\omega_L t + ik_L x\sin\theta)\}$, $\mathbf{E} = \{0, E_y, 0\}$, $\mathbf{k_L} = (\omega_L/c)\{\sin\theta, 0, \cos\theta\}$. Here, ω_L is the laser frequency, c is the light speed, and θ is the incidence angle. For the single component of the electric field envelope $E_y(z, t)$ slowly varying in time, one can write

$$\frac{\partial^2 E_y}{\partial z^2} + k_L^2[\varepsilon(z) - \sin^2\theta]E_y = 0. \tag{1}$$

In the case of *P*-polarization, the single component of the magnetic field envelope $B_y(z, t)$, $\mathbf{B} = \{0, B_y, 0\}$ obeys the following equation:

$$\frac{\partial^2 B_y}{\partial z^2} + k_L^2[\varepsilon(z) - \sin^2\theta]B_y - \frac{\partial \ln\varepsilon(z)}{\partial z}\frac{\partial B_y}{\partial z} = 0. \tag{2}$$

Consider the piecewise constant approximation of the function that describes the complex permittivity of material localized in the range $z_1 \le z \le z_N$, see Fig. 1. The front and back interfaces of the substance are located at $z = z_1$ and $z = z_N$, respectively, the amplitude and phase of the incident electromagnetic wave is determined in the point $z = z_0$. At this approximation, in the arbitrary zone $z_m \le z \le z_{m+1}$ for $m = 0, \ldots, N-1$, Eqs. (1) and (2) have the same form and the type of exact solution

$$F_m(z) = f_m^{(+)} e^{ik_m(z-z_m)} + f_m^{(-)} e^{-ik_m(z-z_m)}, \tag{3}$$

where $F = E_y$ or B_y in the case of *S*- or *P*-polarization, respectively, $f_m^{(+)}$ and $f_m^{(-)}$ are the amplitudes of right and left traveling waves at $z = z_m$, respectively, and $k_m = k_L\sqrt{\varepsilon_m - \sin^2\theta}$ with $k_L = \omega_L/c$. The permittivity is supposed to be constant $\varepsilon(z) = \varepsilon_m$ in the range $z_m \le z \le z_{m+1}$.

Taking in mind the continuity of the tangential field components and first derivative jump for the *P*-polarization, one can write

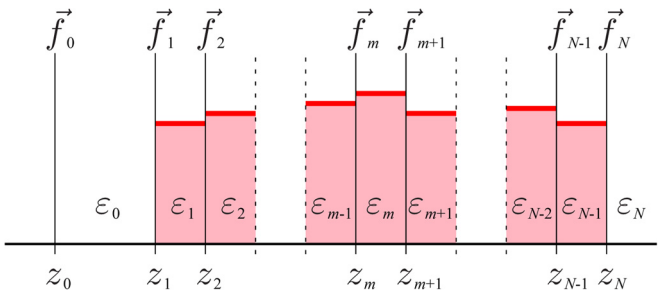

FIG. 1. (Color online) A piecewise constant distribution of permittivity in zones. The electromagnetic field amplitudes $\vec{f}_m$ (10) are determined on zone boundaries.

$$F_m(z_{m+1}) = F_{m+1}(z_{m+1}), \tag{4}$$

$$(\partial F_m/\partial z)|_{z_{m+1}} = D_m(\partial F_{m+1}/\partial z)|_{z_{m+1}}, \tag{5}$$

where

$$D_m = \begin{cases} 1, \text{if } S\text{-polarization}, \\ \varepsilon_m/\varepsilon_{m+1}, \text{if } P\text{-polarization}. \end{cases} \tag{6}$$

Denote the phase $\psi_m = k_m(z_{m+1} - z_m)$ and rewrite the conditions (4) and (5)

$$f_m^{(+)} e^{i\psi_m} + f_m^{(-)} e^{-i\psi_m} = f_{m+1}^{(+)} + f_{m+1}^{(-)}, \tag{7}$$

$$f_m^{(+)} e^{i\psi_m} - f_m^{(-)} e^{-i\psi_m} = \frac{k_{m+1}}{k_m} D_m(f_{m+1}^{(+)} - f_{m+1}^{(-)}). \tag{8}$$

In a vector form, it is equivalent to

$$C_{m+1}\vec{f}_{m+1} = P_m\vec{f}_m, \tag{9}$$

where

$$\vec{f}_m = \begin{pmatrix} f_m^{(+)} \\ f_m^{(-)} \end{pmatrix}, \tag{10}$$

$$C_{m+1} = \begin{pmatrix} 1 & 1 \\ d_{m+1} & -d_{m+1} \end{pmatrix}, \tag{11}$$

with $d_{m+1} = (k_{m+1}/k_m)D_m$, and

$$P_m = \begin{pmatrix} e^{i\psi_m} & e^{-i\psi_m} \\ e^{i\psi_m} & -e^{-i\psi_m} \end{pmatrix}. \tag{12}$$

Using Eq. (9) for $m = 0, \ldots, N-1$, one can obtain

$$\vec{f}_N = (C_N)^{-1}P_{N-1}\ldots(C_2)^{-1}P_1(C_1)^{-1}P_0\vec{f}_0 \tag{13}$$

with $f_0^{(+)}$ given and $f_N^{(-)} \equiv 0$, since no left traveling wave for $z \ge z_N$. Two unknown values $f_0^{(-)}$ and $f_N^{(+)}$ can be easily found from Eq. (13).

Finally, the laser absorption term in each zone can be written as

$$Q_m = \frac{I(t)k_L\mathrm{Im}\{\varepsilon_m\}}{z_{m+1} - z_m}\int_{z_m}^{z_{m+1}} |\mathbf{E}(z)|^2 dz, \tag{14}$$

where $I(t)$ is the incident laser pulse intensity, and

$$|\mathbf{E}|^2 = \begin{cases} |E_y|^2, \text{if } S\text{-polarization}, \\ |E_x|^2 + |E_z|^2, \text{if } P\text{-polarization}. \end{cases} \tag{15}$$

The field components E_y or B_y are calculated from Eqs. (3) and (9) for $f_0^{(+)} \equiv 1$. The relations between E_x, E_z, and B_y in the *P*-polarization case are $E_x = -i/(\varepsilon k_L)(\partial B_y/\partial z)$,

$E_z = -(B_y \sin\theta)/\varepsilon$. Thus, the laser energy absorption in each zone $z_m \le z \le z_{m+1}$ can be determined from Eq. (14).

Coefficients of reflectivity R and transmission T are also known $R = |f_0^{(-)}/f_0^{(+)}|^2$, $T = |f_N^{(+)}/f_0^{(+)}|^2$.

The optical properties of a metal can be described by the Drude model for temperatures below the Fermi one T_F. In aluminum, which is used in this paper the band-to-band contribution ε_{bb} to permittivity at the normal conditions is dominant.[12] In the present model, the metallic part of permittivity ε_{met} depends on laser wavelength ω_L, material density ρ, ion temperature T_i, and electron temperature T_e. It can be approximated by a sum of the band-to-band contribution and the intraband Drude-like term,

$$\varepsilon_{\text{met}}(\omega_L, \rho, T_i, T_e) = \varepsilon_{bb} + 1 - \frac{n_e}{n_{\text{cr}}(1 + i\nu_{\text{eff}}/\omega_L)}, \quad (16)$$

where n_e is the electron concentration, $n_{\text{cr}} = \omega_L^2 m_e/(4\pi e^2)$ is the critical concentration, m_e and e are the electron mass and charge, respectively, and the effective frequency of collisions is $\nu_{\text{eff}} = \min(\nu_{\text{met}}, \nu_{\max})$.

The frequency of collisions in a metal state is a sum of electron-phonon and electron-electron scattering

$$\nu_{\text{met}} = A_1 k_B T_i/\hbar + A_2 k_B T_e^2/(T_F \hbar). \quad (17)$$

The peak frequency of collisions is limited by the electron free-path between ions so that

$$\nu_{\max} = A_3 \frac{\sqrt{v_F^2 + k_B T_e/m_e}}{r_0}, \quad (18)$$

where r_0 is the interatomic distance, v_F is the Fermi electron speed, and k_B is the Boltzmann constant.

For hot states at $T_e \gg T_F$, the plasma model is used in the form[13]

$$\varepsilon_{\text{pl}}(\omega_L, \rho, T_e) = 1 - \frac{n_e}{n_{\text{cr}}}[K_1(\xi) - i(\nu_{\text{pl}}/\omega_L)K_2(\xi)]. \quad (19)$$

Here functions $K_1(\xi) = \frac{8}{3\sqrt{\pi}} \int_0^\infty \frac{t^{10}\exp(-t^2)}{t^6 + x^2} \mathrm{d}t$, $K_2(\xi) = 2\int_0^\infty \frac{t^7 \exp(-t^2)}{t^6 + x^2} \mathrm{d}t$ with $\xi = 3\sqrt{\pi}\nu_{\text{pl}}/(4\omega_L)$ are described in Ref. 14. The expression for the plasma frequency has a form

$$\nu_{\text{pl}} = \frac{4\sqrt{2\pi}}{3} \frac{\langle Z \rangle n_e e^4 \Lambda}{\sqrt{m_e}(k_B T_e)^{3/2}}, \quad (20)$$

where $\langle Z \rangle = n_e/n_i$ is the mean ion charge with concentration of ions n_i, and Λ is the Coulomb logarithm[15]

$$\Lambda = \max\left\{2, \ln\left(\frac{b_{\max}}{b_{\min}}\right)\right\}, \quad (21)$$

$$b_{\max} = \max\left\{r_0, \sqrt{\frac{k_B T_e}{4\pi n_e e^2}}\right\}, \quad (22)$$

$$b_{\min} = \max\left\{\frac{\langle Z \rangle e^2}{k_B T_e}, \frac{\hbar}{\sqrt{m_e k_B T_e}}\right\}. \quad (23)$$

We suppose that the metal–plasma transition occurs in the vicinity of the Fermi temperature and thus we can interpolate between these two states to describe permittivity $\varepsilon(\omega_L, \rho, T_i, T_e)$ in the wide-range of parameters so that

$$\varepsilon = \varepsilon_{\text{pl}} + (\varepsilon_{\text{met}} - \varepsilon_{\text{pl}}) e^{-A_4 T_e/T_F}. \quad (24)$$

In Fig. 2, the permittivity (24) is presented for laser wavelength 1.053 μm, normal density, and single-temperature case. The coefficients used in the permittivity model are adjusted to meet the room temperature conditions for aluminum[16,17] and describe experiments on self-reflectivity[18] and pump-probe measurements for S- and P-polarization[11] ($A_1 = 4.41$, $A_2 = 0.8$, $A_3 = 0.7$, and $A_4 = 0.2$).

III. HYDRODYNAMIC EQUATIONS

Preliminary estimation of a substance reaction to the laser impact can be done for sufficiently large spot diameter in 1D geometry although the full picture can be obtained in multi-dimensional modeling only. We describe here the evolution of material parameters using the conservation of mass, momentum and energy of electron, and ion subsystems in a single-fluid two-temperature 1D Lagrangian form

$$\frac{\partial(1/\rho)}{\partial t} - \frac{\partial u}{\partial m} = 0, \quad (25)$$

$$\frac{\partial u}{\partial t} + \frac{\partial(P_i + P_e)}{\partial m} = 0, \quad (26)$$

$$\frac{\partial e_e}{\partial t} + P_e \frac{\partial u}{\partial m} = -\gamma_{ei}(T_e - T_i)/\rho + Q_L/\rho + \frac{\partial}{\partial m}\left(\rho \kappa_e \frac{\partial T_e}{\partial m}\right) - \frac{\partial S}{\partial m}, \quad (27)$$

$$\frac{\partial e_i}{\partial t} + P_i \frac{\partial u}{\partial m} = \gamma_{ei}(T_e - T_i)/\rho. \quad (28)$$

Here, m is the mass coordinate, $\mathrm{d}m = \rho \mathrm{d}z$; u is the velocity; P_e and P_i are the pressures of electrons and ions,

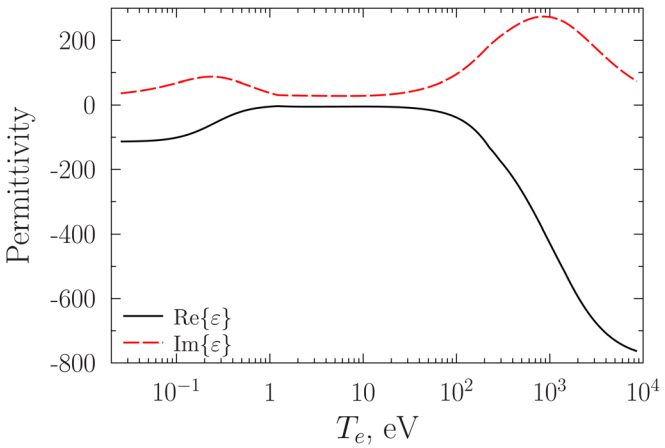

FIG. 2. (Color online) Interpolation formula (24) for the real (solid (black) curve) and imaginary (dashed (red) curve) parts of permittivity for normal density of aluminum 2.71 g/cm^3, laser wavelength 1.053 μm, and $T_i = T_e$.

respectively; e_e and e_i are the specific energies of electrons and ions, respectively. The energy exchange between electrons and ions is described in our model by the corresponding term with coupling coefficient γ_{ei}. The laser energy absorption by the electrons is taken into account using the heat source term Q_L, see Eq. (14). The electron wide-range thermal conductivity coefficient κ_e is used to represent the electron heat transport in the Fourier form. The integral over the spectrum density of the thermal radiation flux S used in Eq. (27) is described in Sec. IV.

To close the system (25)–(28) by relations $P_e(\rho, T_e)$, $P_i(\rho, T_i)$, $e_e(\rho, T_e)$, $e_i(\rho, T_i)$, we use the semiempirical two-temperature multiphase equation of state (EOS) for aluminum[19,20] with the Thomas–Fermi expression for the thermal contribution of electrons[21] instead of the ideal Fermi-gas approximation used in earlier versions of EOS. The equilibrium mean charge of ions $\langle Z \rangle$ is also known from the electron part of EOS and is used in models of transport coefficients. Thus obtained values of $\langle Z \rangle$ are similar to interpolation formula (52) in paper.[22]

The EOS is constructed so that the total free energy has a form $\mathcal{F}(\rho, T_i, T_e) = \mathcal{F}_i(\rho, T_i) + \mathcal{F}_e(\rho, T_e)$, composed of two parts. The first item $\mathcal{F}_i(\rho, T_i) = \mathcal{F}_c(\rho) + \mathcal{F}_a(\rho, T_i)$, in turn, consists of electron-ion interaction term $\mathcal{F}_c$ (calculated at $T_i = T_e = 0$ K) and contribution of thermal motion of ions $\mathcal{F}_a$. An analytical form of $\mathcal{F}_i$ has different expressions for solid and fluid phases.[23] The tables of thermodynamic parameters are calculated taking into consideration an information about phase transitions and metastable regions.[24–26] The second term $\mathcal{F}_e(\rho, T_e)$ is the thermal contribution of electrons described by the Thomas-Fermi model.[21]

Our EOS contains about 40 empirical constants adjusted so that the EOS meets the following requirements: (i) to describe available experimental results on compression and expansion at $T_e = T_i$ for a wide range of densities and temperatures including data on critical and triple points; (ii) to satisfy necessary asymptotes; and (iii) to represent changes of thermodynamic parameters in phase transitions.

The wide-range heat conduction coefficient and coupling parameter are described in detail in Ref. 11. The basic well-established idea[27] is to use an interpolation between limiting metal and hot plasma cases so that the model consists of three branches. The first one describes the metal state from the normal density and room temperature to near-Fermi temperatures. The model in this first region is adjusted using free coefficients[11] to meet both the room temperature handbook data and Vienna Ab initio Simulation Package (VASP) findings.[28,29] Then, the second branch is governed by the maximal frequency of collisions (18) and limits the conductivity and coupling parameter. Finally, the third branch corresponds to the classical hot plasma limit of Spitzer[30] for $T_e \gg T_F$.

IV. RADIATION TRANSPORT

We take into account the thermal radiation energy flux in a diffusion approximation. In 1D case, one can write

$$\frac{\partial S_\omega}{\partial z} = 4\pi j_\omega - \kappa_\omega c U_\omega, \tag{29}$$

$$S_\omega = -\frac{c}{3\kappa_\omega}\frac{\partial U_\omega}{\partial z}, \tag{30}$$

$$S_\omega|_\Omega = \mp\frac{cU_\omega}{2}, \tag{31}$$

where S_ω is the radiation flux density, U_ω is the radiant energy density, j_ω and κ_ω are the coefficients of radiation and absorption, respectively, and Ω is the external boundary of plasma. The integral over the spectrum density of the radiation flux used in Eq. (27) is $S = \int_\omega S_\omega d\omega$.

The system (29)–(31) in a group approximation can be transformed to the diffusion equation with appropriate boundary conditions so that

$$\frac{\partial}{\partial z}\left(-\frac{c}{3\kappa^R_{g_i}}\frac{\partial U_{g_i}}{\partial z}\right) = 4\pi j_{g_i} - \kappa^P_{g_i} c U_{g_i}. \tag{32}$$

Here index g_i denotes the heat radiation frequency range $\omega_i \le \omega \le \omega_{i+1}$ for $i = 1, \ldots, N_g$, where N_g is the number of groups ($N_g = 96$ in the presented below results), $\kappa^R_{g_i}$ and $\kappa^P_{g_i}$ are the mean Rosseland and Planck absorption coefficients, respectively.

Tables of coefficients $\kappa^R_{g_i}$, $\kappa^P_{g_i}$, and j_{g_i} are calculated by algorithms from book.[31] For instance, the absorption coefficient is estimated as

$$\kappa_\omega = \sum_{ks\gamma J} n_{ks\gamma J} \sum_{ks'\gamma' J'} \sigma^{bb}_{ks\gamma J, ks'\gamma' J'}(\omega) + \sum_{ks\gamma J} n_{ks\gamma J}\sigma^{bf}_{ks\gamma J}(\omega) + n_i \sigma^{ff}(\omega), \tag{33}$$

where $n_{ks\gamma J}$ is the concentration of k-fold ions in the state s on atomic level γ and with the moment J; $\sigma^{bb}_{l,m}$, σ^{bf}_m, σ^{ff} are the absorption cross sections of band-to-band transitions, photoionization, and bremsstrahlung, respectively. The summation over indexes k, s', γ', and J' is performed for energies $E_{ks\gamma J} < E_{ks'\gamma' J'}$. Calculation of the emittance coefficient j_ω is done in a similar way.

V. RESULTS AND DISCUSSION

Series of simulations are performed for the laser pulses with wavelength $\lambda_L = 1.053$ μm and typical intensity contrast ratio of nanosecond prepulse $C_{\rm ns} = 10^{-8}$, see Ref. 4. The main pulse is assumed to be Gaussian with different peak intensities $10^{19} \le I_{\max} < 10^{20}$ W/cm^2, and full width at half maximum (FWHM) pulse duration is $\tau_0 = 0.5$ ps. The picosecond-scale prepulse appearing just before the main pulse is also Gaussian with FWHM duration $\tau_1 = 20$ ps and contrast ratio $C_{\rm ps} = 10^{-4}$. Thus, the laser intensity time profile is modeled by formula

$$I(t) = I_{\max}\{C_{\rm ns} + C_{\rm ps}\exp[-\ln(16)t^2/\tau_1^2] + \exp[-\ln(16)t^2/\tau_0^2]\}. \tag{34}$$

These parameters correspond particularly to the petawatt high-energy laser for heavy ion experiments (PHELIX), which is planning to be used for x-ray generation.[32]

In numerical experiment, the aluminum foil of thickness 0.1 μm is irradiated by the right-traveling laser pulse with intensity profile (34) during the time interval $-2000 \le t \le 10$ ps. We intentionally analyze the normal incidence of the pulse that is just determined by the specific geometry of planned experiments. Initially, the front and back foil interfaces are located at 0 and 0.1 μm positions, respectively. Our aim is to analyze a possibility to use the foil for shielding of the main target from the laser prepulse action. To this end, we calculate the laser intensity transmitted through the foil for four peak intensities $I_{\max} = (1;3;5;7) \times 10^{19}$ W/cm^2. The results are shown in Fig. 3 and in more detail in the vicinity of the main pulse in Fig. 4.

It is seen in Fig. 3 that the initial transmission increases due to the electron subsystem heating and corresponding permittivity changes for all laser intensities. Then at $t \gtrsim -1900$ ps, the transmission drops to a negligible values and at $t \approx -500$ ps, it rises again. To explain these processes, consider the evolution of the plasma parameters for presented pulse intensities.

For all four pulse intensities and $t \gtrsim -1900$ ps, the thermodynamic and optical parameters of the plasma correspond to a rather hot and dense matter state with a supercritical electron density, see Figs. 5(a) and 6(a) for moment $t = -995$ ps. This plasma is non-transparent for the prepulse laser field [see solid (black) profiles of normalized electron density]. The non-zero values of the transmitted laser radiation for $-1900 \lesssim t \lesssim -500$ ps in Fig. 3 are determined by the accuracy of the solution to Eq. (9) that is of the order of 10^{-9}.

Starting from moment $t \approx -500$ ps, the transmitted intensity grows, see Fig. 3. The reason is in substantial rarefaction of the foil material when the peak electron density is close to the critical value [Figs. 5(a) and 6(a) for moment $t = -512$ ps] and below the critical value [Figs. 5(a) and 6(a)

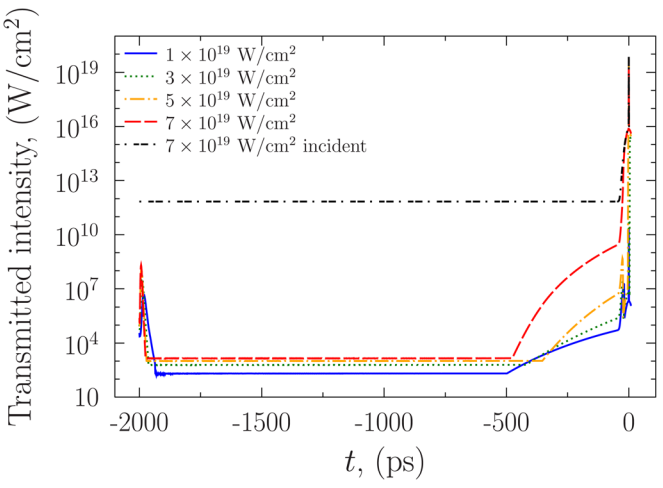

FIG. 3. (Color online) Transmitted intensity $I(t) \times T(t)$ after propagation through the foil for several peak intensities of the main pulse: $I_{\max} = 1 \times 10^{19}$ W/cm^2—solid (blue) curve; $I_{\max} = 3 \times 10^{19}$ W/cm^2—dotted (green) curve; $I_{\max} = 5 \times 10^{19}$ W/cm^2—dashed-and-dotted (orange) curve; $I_{\max} = 7 \times 10^{19}$ W/cm^2—dashed (red) curve. Incident profile for $I_{\max} = 7 \times 10^{19}$ W/cm^2 is also presented by dashed-dashed-dotted (black) line.

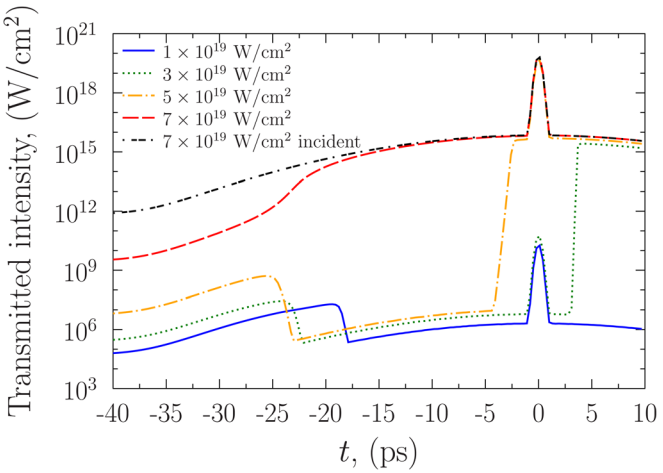

FIG. 4. (Color online) As in Fig. 3 but in the vicinity of the main pulse.

for moment $t = -30$ ps], while the electron temperature is about 60 eV [Fig. 5(c)] for $I_{\max} = 1 \times 10^{19}$ W/cm^2 and is about 200 eV [Fig. 6(c)] for $I_{\max} = 7 \times 10^{19}$ W/cm^2. The ion temperature differs from the electron one in the front and back zones of low-density plasma where the coupling parameter drops with the collision frequency (20), compare panels (c) and (d) in Figs. 5 and 6.

At later time, $t > -30$ ps, when the picosecond prepulse, and then the main pulse, arrives upon the target, the foil

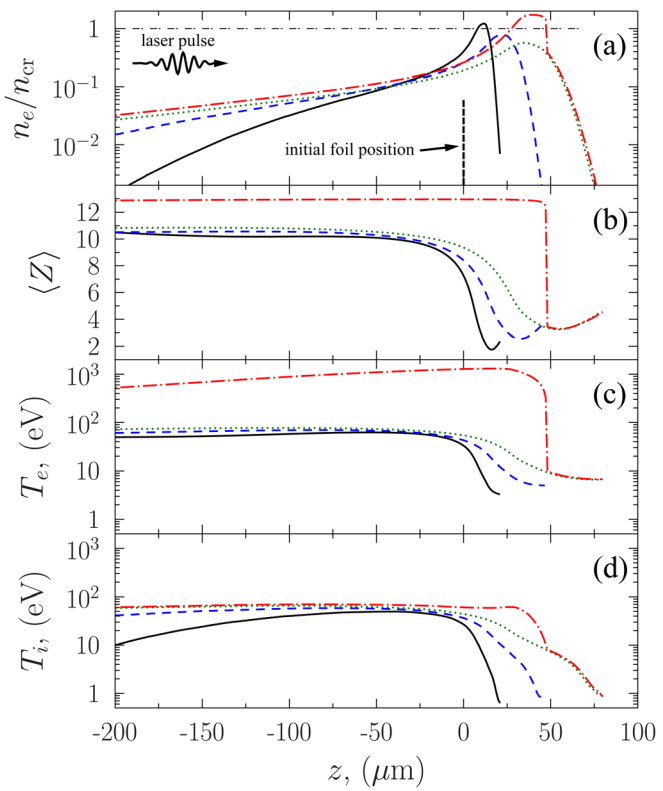

FIG. 5. (Color online) Evolution of the main parameters in the foil for laser pulse with $I_{\max} = 1 \times 10^{19}$ W/cm^2. Electron density normalized to the critical one (a); mean charge of ions (b); electron temperature (c); and ion temperature (d). Instants: solid (black) curve −995 ps; dashed (blue) curve −512 ps; dotted (green) curve −30 ps; dash-and-dot (red) curve −10 ps. The initial foil position is marked by arrow in panel (a).

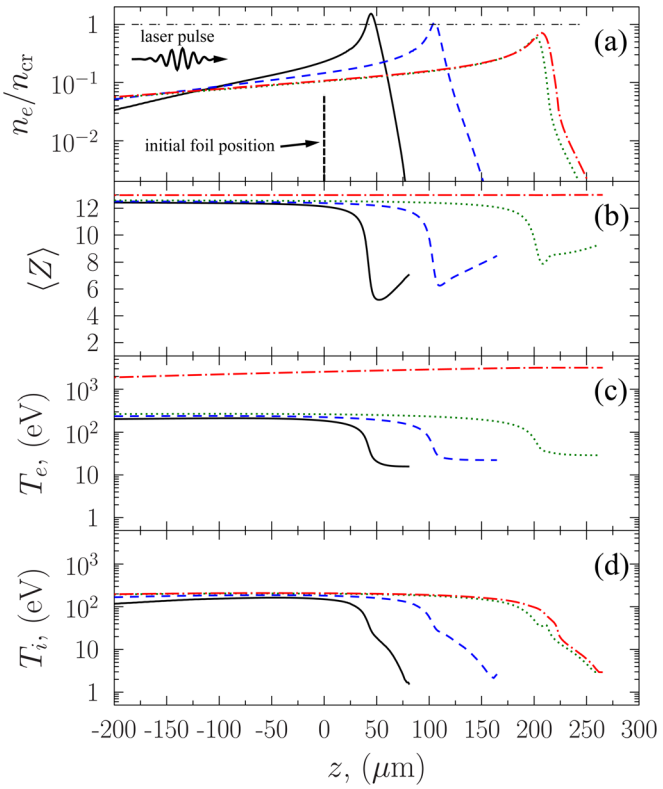

FIG. 6. (Color online) The same as in Fig. 5 but for laser pulse with $I_{max} = 7 \times 10^{19}$ W/cm^2.

dynamics and its transparency depend substantially on the pulse intensity, see Fig. 4. For relatively low intensity, $I_{max} = 1 \times 10^{19}$ W/cm^2, the electron density grows again and reaches the overcritical value [see Fig. 5(a)] because of intensive ionization process in plasma with more than triple increase of $\langle Z \rangle$ (from 4 to 13), see Fig. 5(b) for $t = -30$ and $t = -10$ ps at $z \approx 40$ μm. The electron temperature achieves $\sim$1 keV in this process. Such dynamics explains the drop in transmitted intensity clearly seen in Fig. 4 for moments between -25 and -5 ps for the peak laser intensities $\leq 5 \times 10^{19}$ W/cm^2.

The other time evolution of the plasma parameters is observed for the laser pulse with peak intensity $I_{max} = 7 \times 10^{19}$ W/cm^2. As a consequence of high electron temperature $\sim$100 eV, the mean ion charge is $\sim$9 for moment $t = -30$ ps in the vicinity of electron density maximum $z \approx 200$ μm. The subsequent ionization observed at $t = -10$ ps is close to its maximal value 13 for aluminum, Fig. 6(b). This growth of charge results in $\sim$50% electron density increase which, however, remains below the critical value. Due to this reason, the very hot [up to 3.5 keV, see Fig. 6(c)] and undercritical plasma is almost completely transparent for the main pulse, see Fig. 4, dashed (red) curve.

Varying the thickness of the foil, one can adjust the moment when the foil plasma becomes transparent and thus diminish the undesirable action of the prepulse of given intensity and duration. The results illustrated in Fig. 4 for $I_{max} = 5 \times 10^{19}$ W/cm^2 show a possibility to improve the laser contrast in many orders of magnitude even for a picosecond-scale laser prepulse. Of course, as the rarefaction

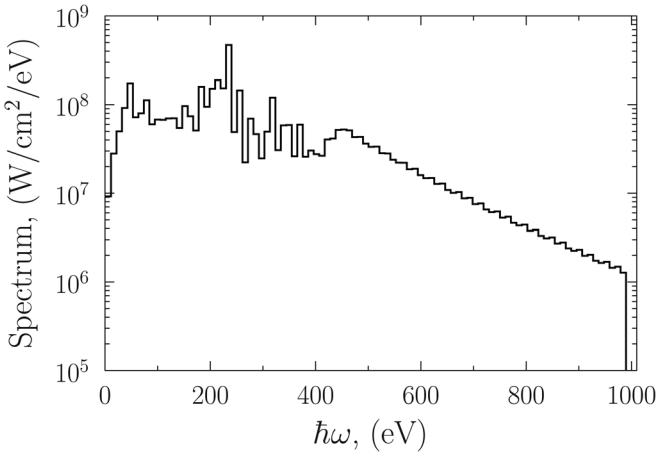

FIG. 7. Spectrum of re-emission S_ω (30) with 96 groups in the target direction (right) for moment $t = -995$ ps and for $I_{max} = 7 \times 10^{19}$ W/cm^2.

of the target during the action of the nanosecond prepulse is a 3D-process, our 1D calculations give only approximate estimation of this transparency moment. In 3D case, one would expect this event to occur earlier. Nevertheless this simple prepulse elimination technique can be used in experiments with a relatively low contrast ratio of the laser pulse.

The possible difficulty in realization of the prepulse cutoff scheme with the aid of a thin metal foil is the laser energy transformation into the thermal radiation. The spectrum of the right-traveling radiation flux (on the back side of the foil) is presented in Fig. 7 for characteristic moment $t = -995$ ps and intensity $I_{max} = 7 \times 10^{19}$ W/cm^2. The dominating spectral range for the output flux is close to 200 eV (soft x-ray). This soft radiation is absorbed more effectively in solid targets in comparison with the laser light. Note, that neglecting of σ^{bb} and σ^{bf} in Eq. (33) (i.e., the bremsstrahlung only) leads to underestimation of radiation energy losses and up to twice higher foil temperature.

Our modeling results show that the hot plasma radiation flux indeed can be quite intensive and sufficient to heat the target placed behind the foil although the laser beam itself

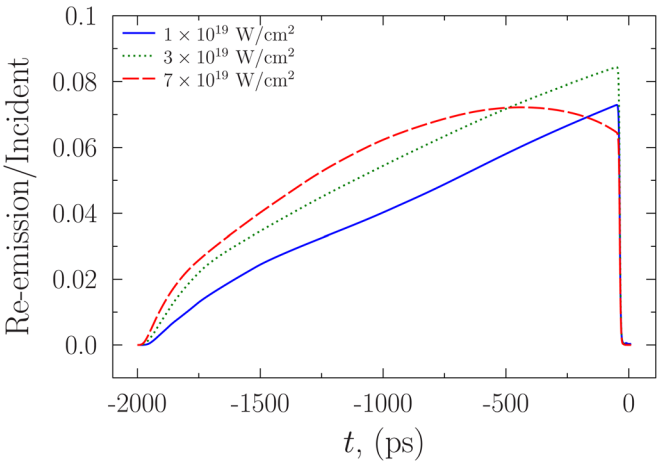

FIG. 8. (Color online) Thermal radiation flux S behind the foil normalized to incident laser intensity for different peak intensities: $I_{max} = 1 \times 10^{19}$ W/cm^2—solid (blue) curve; $I_{max} = 3 \times 10^{19}$ W/cm^2—dotted (green) curve; $I_{max} = 7 \times 10^{19}$ W/cm^2—dashed (red) curve.

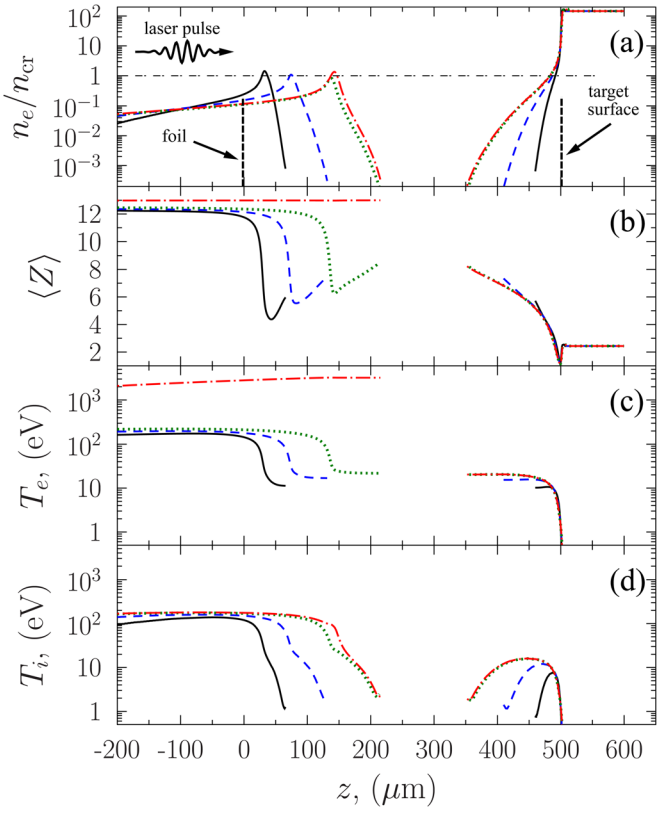

FIG. 9. (Color online) Evolution of the main parameters in the foil and target of aluminum for laser pulse with $I_{max} = 5 \times 10^{19}$ W/cm^2. Instants as in Fig. 5. Initial foil and target positions are marked by arrows in panel (a).

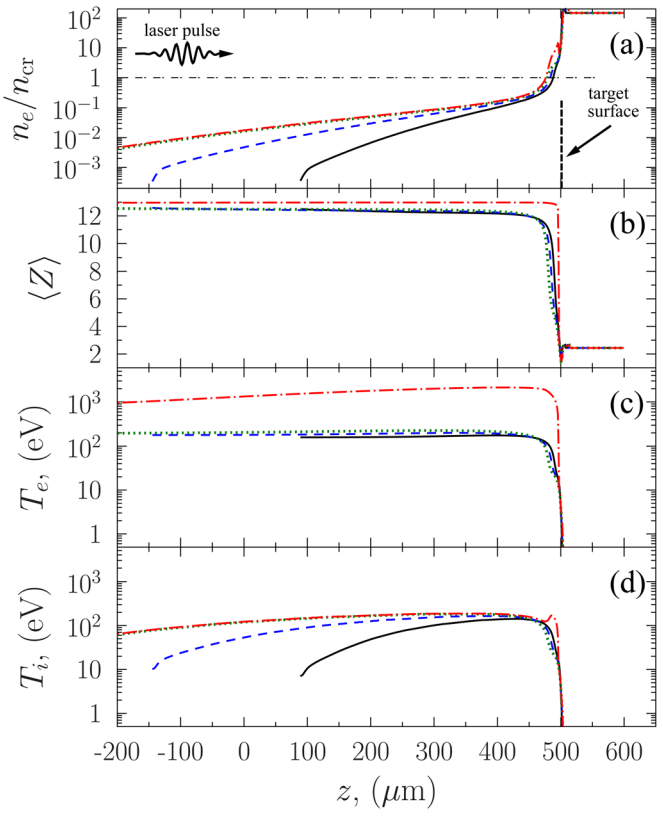

FIG. 10. (Color online) As in Fig. 9 but without foil.

may not reach it. The re-emission in the direction of the target reaches up to 7% of the incident laser energy, see Fig. 8. This heat radiation penetrates into the target and warms it up. The direct simulation of this process for $I_{max} = 5 \times 10^{19}$ W/cm^2, which is the optimal run in terms of maximal target screening, is presented in Fig. 9.

The shielding foil is initially located at $0 \le z \le 0.1$ μm and the bulk target of aluminum is placed behind the foil so that it occupies $500 \le z \le 600$ μm. The gap of $\sim$500 μm between the foil and target helps to avoid the hydrodynamic interaction between them during the simulation. It is seen that the re-emission radiation flux results in the target material expansion $\sim$50 μm by moment -995 ps. The position of the critical electron density is situated at 10, 13, and 17 μm away from the initial target surface position for instants -995, -512, and -30 ps, respectively, see Fig. 9(a). The characteristic temperature of electrons and ions in the near-surface plasma is about 20 eV during the prepulse action. This target preheating is the result of thermal radiation action only since the laser beam does not reach the target till the moment $t = -5$ ps, see dashed-and-dotted (orange) curve in Fig. 4. As one can see in Fig. 9, there is no visible difference in target plasma parameters for moments -30 and -10 ps, while the foil plasma demonstrates a sizable growth of $\langle Z \rangle$ and T_e. The ionization minimum at $z \approx 500$ μm in Fig. 9(b) is connected with the formation of strongly coupled degenerate plasma near the surface of the target. Thus, for the described parameters, some target preheating takes place despite the laser light screening and may result in early smearing of the sub-micron structured targets. Besides, the main pulse propagation through the foil plasma may be changed by the relativistic self-focusing effect.[33] However, this substantially 3D phenomenon cannot be described in the framework of our 1D model.

Simulation without the shielding foil demonstrates much more intensive heating and expansion of the target, see Fig. 10. The leading plasma edge at the moment -30 ps reaches the position ~ -400 μm and the entire plasma extent is about 900 μm that is much larger than $\sim$150 μm for the shielded target.

To remedy the problem of the prepulse energy re-emission by the shielding foil and consequent undesirable heating and rarefaction of the main target, one can use the foil material with less nuclear charge (light elements or compounds like CH or CH_2 to reduce the integral radiation flux in the direction of the target) and also increase the gap between the foil and the target. These simulations are in sight.

VI. CONCLUSIONS

In summary, we have used the developed two-temperature single-fluid hydrodynamic model for investigation of dynamics of thin metal foils irradiated by high-intensity laser pulses with moderate contrast. The model describes accurately the laser field propagation and absorption, employs wide-range transport and optical properties, radiation transport, and EOS of the material that is of high importance for correct simulation of a thin target expansion

starting from the normal conditions. With this model, we have studied the action of nanosecond prepulse of the powerful ultra-short laser on the aluminum foil. The fraction of the laser energy transmitted through the foil is determined together with the estimation of emitted thermal radiation flux.

We have found out that by variation of the foil thickness, one can provide the total transparency of the foil for the main high-intensity ultra-short laser pulse and substantially (in orders of magnitude) diminish the prepulse transmitted through the foil. At the same time, the re-emission of the prepulse energy by the shielding foil can be significant producing an undesirable heating and rarefaction of the target placed behind the foil. Additional calculations should help to adjust shield parameters and reduce the action of the foil plasma re-emission.

ACKNOWLEDGMENTS

We thank Professor V. G. Novikov and D. A. Kim for supplying us with the tables of radiation coefficients and radiation transport program module.

This work was supported by the Russian Foundation for Basic Research (Project Nos. 09-08-01129, 11-02-12217 and 11-08-01225), the Council of the President of the Russian Federation for Support of Young Russian Scientists and Leading Scientific Schools (Grant No. NSh-7241.2012.2), and the Ministry of Education and Science of the Russian Federation (the Federal targeted program "Research and development in priority fields of scientific and technological complex of Russia" 2007–2013, Contract No. 07.514.12.4002).

[1]T. Ditmire, S. Bless, G. Dyer, A. Edens, W. Grigsby, G. Hays, K. Madison, A. Maltsev, J. Colvin, M. J. Edwards, R. W. Lee, P. Patel, D. Price, B. A. Remington, R. Sheppherd, A. Wootton, J. Zweiback, E. Liang, and K. A. Kielty, Radiat. Phys. Chem. **70**, 535 (2004).

[2]U. Zastrau, P. Audebert, V. Bernshtam, E. Brambrink, T. Kämpfer, E. Kroupp, R. Loetzsch, Y. Maron, Y. Ralchenko, H. Reinholz, G. Röpke, A. Sengebusch, E. Stambulchik, I. Uschmann, L. Weingarten, and E. Förster, Phys. Rev. E **81**, 026406 (2010).

[3]D. C. Carroll, O. Tresca, R. Prasad, L. Romagnani, P. S. Foster, P. Gallegos, S. Ter-Avetisyan, J. S. Green, M. J. V. Streeter, N. Dover, C. A. J. Palmer, C. M. Brenner, F. H. Cameron, K. E. Quinn, J. Schreiber, A. P. L. Robinson, T. Baeva, M. N. Quinn, X. H. Yuan, Z. Najmudin, M. Zepf, D. Neely, M. Borghesi, and P. McKenna, New J. Phys. **12**, 045020 (2010).

[4]Y. Kitagawa, H. Fujita, R. Kodama, H. Yoshida, S. Matsuo, T. Jitsuno, T. Kawasaki, H. Kitamura, T. Kanabe, S. Sakabe, K. Shigemori, N. Miyanaga, and Y. Izawa, IEEE J. Quantum Electron. **40**, 281 (2004).

[5]V. Bagnoud and F. Salin, IEEE J. Sel. Top. Quantum Electron. **4**, 445 (1998).

[6]V. Bagnoud, B. Aurand, A. Blazevic, S. Borneis, C. Bruske, B. Ecker, U. Eisenbarth, J. Fils, A. Frank, E. Gaul, S. Goette, C. Haefner, T. Hahn, K. Harres, H.-M. Heuck, D. Hochhaus, D. Hoffmann, D. Javorkov, H.-J. Kluge, T. Kuehl, S. Kunzer, M. Kreutz, T. Merz-Mantwill, P. Neumayer, E. Onkels, D. Reemts, O. Rosmej, M. Roth, T. Stoehlker, A. Tauschwitz, B. Zielbauer, D. Zimmer, and K. Witte, Appl. Phys. B: Lasers Opt. **100**, 137 (2010).

[7]G. Doumy, F. Quéré, O. Gobert, M. Perdrix, P. Martin, P. Audebert, J. C. Gauthier, J.-P. Geindre, and T. Wittmann, Phys. Rev. E **69**, 026402 (2004).

[8]P. McKenna, F. Lindau, O. Lundh, D. Neely, A. Persson, and C.-G. Wahlström, Philos. Trans. R. Soc. A **364**, 711 (2006).

[9]A. V. Ovchinnikov, O. F. Kostenko, O. V. Chefonov, O. N. Rosmej, N. E. Andreev, M. B. Agranat, J. L. Duan, J. Liu, and V. E. Fortov, Laser Part. Beams **29**, 249 (2011).

[10]D. Neely, P. Foster, A. Robinson, F. Lindau, O. Lundh, A. Persson, C.-G. Wahlström, and P. McKenna, Appl. Phys. Lett. **89**, 021502 (2006).

[11]M. E. Povarnitsyn, N. E. Andreev, E. M. Apfelbaum, T. E. Itina, K. V. Khishchenko, O. F. Kostenko, P. R. Levashov, and M. E. Veysman, Appl. Surf. Sci. (in press).

[12]B. Hüttner, J. Phys.: Condens. Matter **8**, 11041 (1996).

[13]M. Veysman, B. Cros, N. Andreev, and G. Maynard, Phys. Plasma **13**, 053114 (2006).

[14]N. Andreev, M. Veysman, V. Efremov, and V. Fortov, High Temp. **41**, 594 (2003).

[15]O. F. Kostenko and N. E. Andreev, "The kinetic model of laser plasma," presented at XIII International Conference on Physics of Non-Ideal Plasmas, Chernogolovka, Russia, 13–18 September 2009, http://www.ficp.ac.ru/pnp/presentations/PNP13-Kostenko.pdf.

[16]*Handbook of Optical Constants of Solids I*, edited by E. D. Palik (Academic, New York, 1985).

[17]K. Widmann, G. Guethlein, M. E. Foord, R. C. Cauble, F. G. Patterson, D. F. Price, F. J. Rogers, P. T. Springer, R. E. Stewart, A. Ng, T. Ao, and A. Forsman, Phys. Plasmas **8**, 3869 (2001).

[18]D. F. Price, R. M. More, R. S. Walling, G. Guethlein, R. L. Shepherd, R. E. Stewart, and W. E. White, Phys. Rev. Lett. **75**, 252 (1995).

[19]M. E. Povarnitsyn, T. E. Itina, M. Sentis, P. R. Levashov, and K. V. Khishchenko, Phys. Rev. B **75**, 235414 (2007).

[20]M. E. Povarnitsyn, K. V. Khishchenko, and P. R. Levashov, Appl. Surf. Sci. **255**, 5120 (2009).

[21]O. P. Shemyakin, P. R. Levashov, L. R. Obruchkova, and K. V. Khishchenko, J. Phys. A: Math. Theor. **43**, 335003 (2010).

[22]P. Fromy, C. Deutsch, and G. Maynard, Phys. Plasmas **3**, 714 (1996).

[23]K. V. Khishchenko, J. Phys.: Conf. Ser. **121**, 022025 (2008).

[24]K. V. Khishchenko, S. I. Tkachenko, P. R. Levashov, I. V. Lomonosov, and V. S. Vorob'ev, Int. J. Thermophys. **23**, 1359 (2002).

[25]V. I. Oreshkin, R. B. Baksht, N. A. Ratakhin, A. V. Shishlov, K. V. Khishchenko, P. Levashov, and I. I. Beilis, Phys. Plasmas **11**, 4771 (2004).

[26]P. R. Levashov and K. V. Khishchenko, AIP Conf. Proc. **955**, 59 (2007).

[27]K. Eidmann, J. Meyer-ter-Vehn, T. Schlegel, and S. Hüller, Phys. Rev. E **62**, 1202 (2000).

[28]V. Recoules and J.-P. Crocombette, Phys. Rev. B **72**, 104202 (2005).

[29]Z. Lin, L. V. Zhigilei, and V. Celli, Phys. Rev. B **77**, 075133 (2008).

[30]L. Spitzer and R. Härm, Phys. Rev. **89**, 977 (1953).

[31]A. F. Nikiforov, V. G. Novikov, and V. B. Uvarov, *Quantum-Statistical Models of Hot Dense Matter: Methods for Computation Opacity and Equation of State* (Birkhäusen Verlag, Basel–Boston–Berlin, 2005).

[32]V. Bagnoud, private communication (2011).

[33]P. Monot, T. Auguste, P. Gibbon, F. Jakober, G. Mainfray, A. Dulieu, M. Louis-Jacquet, G. Malka, and J. L. Miquel, Phys. Rev. Lett. **74**, 2953 (1995).